



## Vortex generation and flow pattern development after a solitary wave passing over a bottom cavity

Chih-Hua Chang <sup>a,\*</sup>, Chii-Jau Tang <sup>b</sup>, Chang Lin <sup>c</sup>

<sup>a</sup> Department of Information Management, Ling-Tung University, Taichung 408, Taiwan, ROC

<sup>b</sup> Department of Hydraulics and Ocean Engineering, National Cheng Kung University, Tainan 70101, Taiwan, ROC

<sup>c</sup> Department of Civil Engineering, National Chung Shin University, Taichung 402, Taiwan, ROC

### ARTICLE INFO

#### Article history:

Received 28 November 2010

Received in revised form 13 August 2011

Accepted 19 September 2011

Available online 29 September 2011

#### Keywords:

Wave–cavity interaction

Solitary wave

Flow visualization

Vortex flow

Streamfunction

### ABSTRACT

Several vortices are generated immediately inside the cavity for a short duration when a solitary wave passes over a bottom cavity in shallow water. Afterward, the primary vortex grows gradually in size and then is transported outward to breed another counter-rotating vortex to form a jet in the tranquil environment. In this study, a two-dimensional streamfunction–vorticity model was treated in a transient grid to conform the free surface and formulated by the Finite Analytic (FA) discretization to seek a time-accurate numerical solution. We used an overset grid to refine the small region around the cavity to improve the solution accuracy and obtain computational efficiency in the analysis. The model was first validated for a quasi-steady boundary-layer flow, induced by a solitary wave passing over a flat bottom, through the comparison of velocity profiles with Liu et al. [J Fluid Mech 2007;574:449–63]. Then, the evolved vortical flow for the cavity problem was investigated under the effects of various sizes of a cavity and various amplitudes of the incident solitary wave. These simulated results showed consistent agreement in the evolved vortex patterns with the visualization experiment in laboratory.

Crown Copyright © 2011 Published by Elsevier Ltd. All rights reserved.

## 1. Introduction

The flow induced by a solitary wave passing over a flat bottom is almost horizontal and uniform throughout the water depth. By “almost”, we mean that the variation of both vertical velocity and uniformity of horizontal velocity in depth is of order  $O(\mu^2)$  or, equivalently, of  $O(\varepsilon)$ . Here we signify the wave dispersion by the parameter  $\mu^2$  ( $\equiv H^2/L^2$ ) and the nonlinearity by  $\varepsilon$  ( $\equiv A/H$ ), for the amplitude  $A$  and characteristic wave length  $L$  of a solitary wave and the undisturbed water depth  $H$ . The equal order of  $O(\mu^2)$  and  $O(\varepsilon)$  mentioned above is consistent with the counterbalance between dispersion and nonlinearity of a solitary wave so its waveform is preserved during propagation. At a particular location, one observes that the induced flow first accelerates from rest when a solitary wave is approaching, then gets to a maximum velocity under the wave crest, and decelerates finally to the zero velocity again as the wave leaves. All fluid throughout the water depth as described above, even inside the bottom boundary layer, will move all the time in the same direction as the wave does, except a reversed flow appears in certain time interval within the deceleration phase. The flow reversibility has already been confirmed in both PIV measurement and numerical analysis performed by Liu

et al. [14]. They also drew the conclusion consequently from their agreed result that the shear stress on bottom changes sign as the flow reverses its direction. Still, it is not clear whether the flow does separate or not from the bottom surface as the pressure gradient is adversely positive in the deceleration phase. We will notice later in this paper that the reversed flow with adverse pressure gradient is not related to flow separation from the bottom but, instead, to the flow attachment to the bottom. Therefore, although the vortex sheet has both positive and negative senses of vorticity generated by the induced flow, it can only thicken the boundary layer and then decay itself gradually by viscous diffusion. There is no way to carry outward the vorticity inside the boundary layer by, for example, a separated flow or else mechanisms to form an isolated vortex or coupled vortices.

However, over an uneven bottom of either convex protrusion or concave cavity, the bottom flow induced by a solitary wave can enforce the immediate separation around the sharp edge. The vortex of concentrated vorticity sheds away immediately from the corner by the separated flow, and the vortical flow further produces an interesting flow pattern in the fluid. On the problem of a solitary wave passing over a bottom protrusion, the separated vortical flow shedding around a submerged rectangular obstacle has been studied previously (for example, by Tang and Chang [23,24], Chang et al. [2], Hsu et al. [7], Lin [11], Lin et al. [9,10], etc.). Surprisingly enough, relatively less study was found in the articles for the vortical flow induced by the solitary wave around the bottom

\* Corresponding author.

E-mail address: changbox@teamail.ltu.edu.tw (C.-H. Chang).

cavity, although this type of flow motion is often observed in nature. In this study, we attempt to investigate the detailed process of how the interactive vortical flow pattern creates around the cavity and how the free surface deforms as the solitary wave transmits over the cavity.

Although the vorticity carried outward from the leading edge of a cavity may be in a similar manner to that from the trailing edge of a protrusion, the former has many distinct subsequent features from the latter. For the protrusion-flow case, the primary vortex, after shedding away from the rear edge of obstacle, is little disturbed by the obstacle (see Tang and Chang [23,24]). On the other hand, for a cavity-flow case, the separated vortical flow makes the peculiar pattern due to its continuous interaction with the surroundings, including the enclosure walls of cavity, outer bottom walls and the free surface. After a short action by the passing solitary wave, such a flow develops several vortices of various sizes to form a lot of locally isolated, recirculating flow subregions around the cavity. Among them, the primary vortex  $V_A$  is not only convected and diffused out of the cavity to increase its own size, but also breeds a new counter-rotating vortex  $V_B$ , slightly weaker in strength, at a little upstream outside the cavity. Other two minor vortices  $V_C$  and  $V_D$  stay at their respective sites, either around the right lower corner inside the cavity or around downstream bottom outside the cavity. The influence of  $V_C$  and  $V_D$  is clearly of no essence on the global flow pattern. Finally, an emerging jet is gradually developed between  $V_A$  and  $V_B$ . With the aid of visualization technique, the stated flow patterns can be observed as well in laboratory, as shown in Fig. 2. The tested model in the laboratory was setup by putting two acrylic rectangles together by a gap to form a submerged cavity above the flume bottom, with two additional outer slopes connected the rectangles to both far flat bottoms to avoid side effects of deforming the incident solitary wave and undesired wave reflection from the tested model. An incident solitary wave is generated by a wave maker for a short distance at the upstream of a flume. Although not so strictly in both its waveform and the cavity model as in our intended study here, the flow pattern shown in photos still provides the meaningful illustration to depict the phenomenon of vortex motion related to the present study. Three stages of vortex motion are seen from these photos in sequence: (a) generation and growth of vortices  $V_A$  and  $V_D$ , (b) transportation of vortex  $V_A$  outward of cavity and (c) jet formation between  $V_A$  and  $V_B$  with companions  $V_C$  and  $V_D$ . The phenomenon similar to these vortical flow patterns will be simulated numerically by using more rigor formulations and flow conditions in the present study.

For previous studies on cavity flows, most investigators usually considered two kinds of flow configuration, namely, either driven by a sliding sidewall in an enclosure cavity, known as lid-driven cavity flow, or driven openly by an outer current with or without

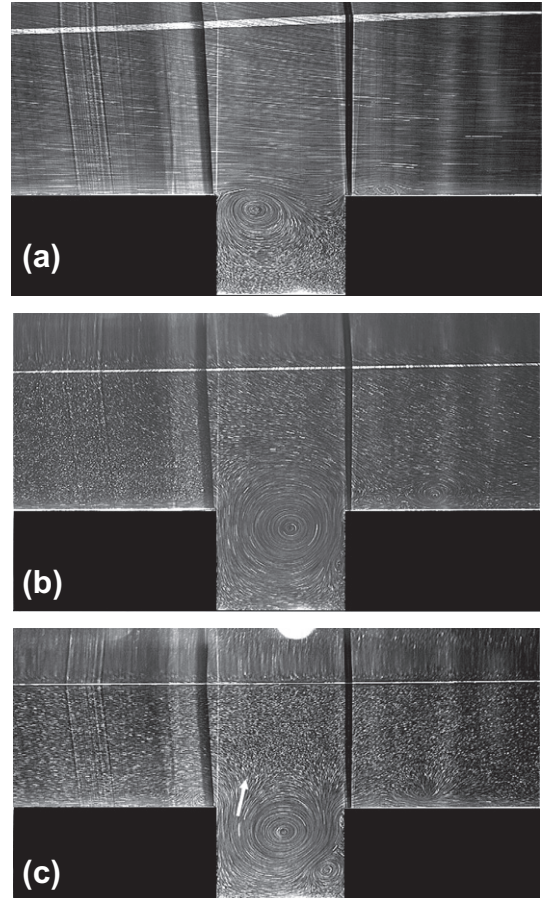


**Fig. 2.** Flow visualization for evolving primary vortex at three stages: (a) growth, (b) transportation, and (c) jet formation.

a free surface, known as open cavity flow. Much effort on both flow problems for various applications has been made; for example, see reviews of Shankar and Deshpande [20], Rowley and Williams [19], and others. Between these two cavity flows, an open cavity flow seems to be more concerned with the present study. However, further study finds that the generated vortices have little chance to be transported out of the open cavity because of suppression under the continuous action of outer flow. Although some vorticity for the open cavity flow could be diffused outward, it is immediately convected downstream by the outer current. Therefore, all vortices can only stay inside the cavity, either kept stationary or oscillating to and fro [1]. The open cavity flow problem is thus quite different from the present study which involves only the short action time for initiation of the vortex generation and the subsequent long duration for interactive evolution in a tranquil environment. Owing to these differences, further discussion of an open cavity flow will not be considered here.

Studies on interaction between nonlinear long waves and coastal structures have attracted long intensive interests to engineers and scientists. Various models for the inviscid free-surface flow field were proposed to fit different degrees of flexibility and accuracy in application, from those long-wave models using the classical KdV or Boussinesq equation(s) to more complete wave-flow models through potential flow or the Euler equations. Moreover, the general viscous flow model using the Navier-Stokes (NS) equations is often used when one attempts to take account of the viscous effects on the flow. Because it is not necessary to introduce any wave theory when applied to a wave problem, a general free-surface flow model like the Euler or NS model requires the

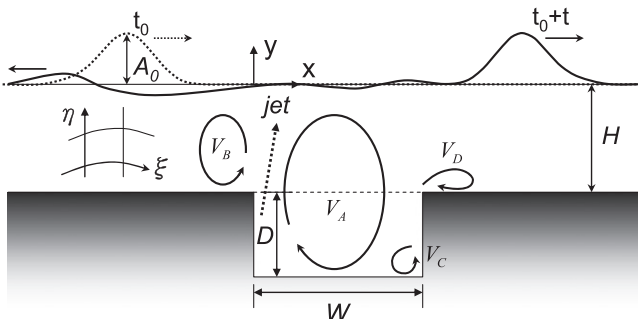


**Fig. 1.** Schematic sketch of studied problem.

high-accuracy solution to compete against the pure wave model. To this end, a general flow model could, however, suffer many difficulties in seeking the accurate numerical solution for the wave-flow field, especially for those models using primitive variables of velocity and pressure. Even without a free surface involved, two main difficulties frequently arise in primitive-variable NS models, namely, one from the nonlinear coupling of convective momentum flux, and the other from the implicit constrain of pressure to satisfy the incompressibility condition from the continuity equation (see, for example, Patankar [17], Tang et al. [22], etc.). In addition, the irregular geometry of a fixed or a moving boundary like the free surface may further worsen these difficulties. To the irregular boundary shape, whether given or determined as a solution, the vector form of velocity degrades seriously the solution quality, either through the interpolation process (when using a Cartesian or regular grid) or through the transformation process (when using a boundary-fitting grid). All these complexities often lead to the solution procedures suffering from inaccuracy and instability problems in practical application.

In 1781, Lagrange introduced a streamfunction to study a two-dimensional (2D) flow of incompressible fluid. More discussions on streamfunctions in the general three-dimensional (3D) flow field can be found in Yih [25]. Due to its simplicity and applicability, many fundamental theories, for instance, the boundary-layer theory, flow stability, etc., and many practical studies by analytic or numerical methods, have applied streamfunction in analyses for years (see more discussion in Gresho [5] and others). Thus, we will use the 2D streamfunction–vorticity ( $\psi$ - $\omega$ ) flow model for it has less solution variables invoked and simpler formulation in grid transformation among all NS flow models. For 2D nonlinear water wave problems with viscous effects to be considered, the fully nonlinear free surface conditions in a boundary-fitting grid have ever been developed in this model [23]. Particularly being applied presently with a more general overset grid system, the transformed governing equations and initial/boundary conditions will be discussed in Section 2. The detailed numerical schemes will be discussed in Section 3, including the discretization method by means of local analytic solution, the base grid and refined overset grid by algebraic generation method and its application to present problem. In Section 4.1, the validation of our numerical model is conducted through the comparison of velocity profile with Liu et al.'s experimental result and numerical solution of boundary-layer approximation [14]. Then, in Section 4.2, we will perform analyses of grid independency and computational efficiency by assessing three overset grids. The evolved free-surface profiles associated with the initiation of vortex generation inside cavity will be simulated in Section 4.3. Section 4.4 will present the detailed study on the consequent development of interactive vortical flow pattern. Finally, the visualized flow pattern again by dye traction is compared with our numerical results. Both show consistent agreement in the evolved vortex patterns at three stages.

## 2. Formulations

### 2.1. Flow equations in an evolved grid system

Consider a 2D, incompressible, viscous fluid flow induced by a solitary wave propagating over a bottom cavity, as illustrated schematically in Fig. 1. Let all flow variables be non-dimensionalized and scaled by the undisturbed-water-depth ( $H^*$ ), the fluid density ( $\rho$ ) and the linear wave speed ( $\sqrt{gH^*}$ ), where  $g$  is the gravitational constant. The flow field modeled by the streamfunction and vorticity, known as streamfunction–vorticity ( $\psi$ - $\omega$ ) formulation, is formulated by

$$\nabla^2\psi = -\omega, \quad (1)$$

$$\frac{D\omega}{Dt} = \frac{\nabla^2\omega}{Re}, \quad (2)$$

where the Reynolds number  $Re = H^*\sqrt{gH^*}/v$  signifies the viscous effects of the fluid induced by wave motion due to kinematic viscosity  $v$ . The material derivative  $D\omega/Dt$  in Eq. (2) is taken in the Lagrangian frame to count for the vorticity variation following a fluid particle. The Poisson Eq. (1) of streamfunction with source  $\omega$  is obtained directly from the definition of vorticity  $\omega$  while the vorticity convective-diffusive transport equation, Eq. (2), is derived by taking the curl of momentum equations to eliminate the pressure gradient.

In this study, the free surface is an unknown moving boundary of time dependence. Therefore, instead of the Cartesian coordinates  $(x, y; t)$ , we prefer using a general time-evolving curvilinear coordinate system  $(\xi, \eta; \tau)$ . This enables us to conform to the evolved free surface all the time by a specified grid line in the most convenient way. In this article, we will use subscripts of  $\xi$ ,  $\eta$  and  $\tau$  denoting the differentiations and  $[., .]$  listing the Cartesian  $x$  and  $y$  components. Consider the position vector  $\mathbf{r}(\xi, \eta; \tau)$  at an arbitrary point, which could be a grid nodal point or a fluid particle in movement. The differential of a small element

$$d\mathbf{r} = \mathbf{r}_\xi d\xi + \mathbf{r}_\eta d\eta + \mathbf{r}_\tau d\tau = \mathbf{g}_1 d\xi + \mathbf{g}_2 d\eta + \mathbf{v}_g d\tau, \quad (3)$$

yields the local moving coordinate system where the covariant base vectors  $\mathbf{g}_1$ ,  $\mathbf{g}_2$  and the velocity  $\mathbf{v}_g$  are defined by the transformations

$$\mathbf{g}_1 = \mathbf{r}_\xi = [x_\xi, y_\xi], \quad \mathbf{g}_2 = \mathbf{r}_\eta = [x_\eta, y_\eta], \quad \mathbf{v}_g = \mathbf{r}_\tau = [x_\tau, y_\tau], \quad (4)$$

Remind that the covariant base vectors are in the directions tangent to  $\xi$  and  $\eta$  grid lines while the contravariant base vectors are normal to the  $\xi$  and  $\eta$  grid surfaces. If the grid system is fixed in space, viz  $\mathbf{v}_g = 0$  for all grid nodes, the reference frame is exactly the Eulerian frame system while, on the other hand, if all grid points move with flow particles at velocity  $\mathbf{v}_g = \mathbf{u}$ , the frame of reference becomes the Lagrangian system. In more general applications, we construct a numerical grid system with arbitrary  $\mathbf{v}_g$  at each node so that the grid can evolve and deform spatially with time under our control. Moreover, for programming convenience, we intentionally assign the integer values of  $\xi$ ,  $\eta$  to represent the corresponding grid lines and to use them as array indices in coding. When the velocity and the location are both specified at all grid points, the local transformation, Eqs. (3) and (4), between  $(x, y; t)$  and  $(\xi, \eta; \tau)$  with  $\tau = t$  can be rewritten by matrix form

$$\begin{bmatrix} dx \\ dy \\ dt \end{bmatrix} = \begin{bmatrix} x_\xi & x_\eta & x_\tau \\ y_\xi & y_\eta & y_\tau \\ 0 & 0 & 1 \end{bmatrix} \begin{bmatrix} d\xi \\ d\eta \\ d\tau \end{bmatrix} = \mathbf{J} \begin{bmatrix} d\xi \\ d\eta \\ d\tau \end{bmatrix}. \quad (5)$$

Here  $\mathbf{J}$  is the Jacobian matrix of transformation whose determinant, known as Jacobian,  $J = x_\xi y_\eta - y_\xi x_\eta$ , represents the area deformation of a grid element in space since  $dA = dx dy = J d\xi d\eta$ . The requirement for existence and uniqueness of transformation is easily met once  $J$  does not vanish. Moreover, because the area has already been taken as one unit in the  $(\xi, \eta)$  domain, the Jacobian is exactly the local area of a grid cell mapping onto the physical  $(x, y)$  domain in deformation. This gives us the great advantage in numerical integration of circulation, as will be discussed later. The inverse transformation,  $\xi = \xi(x, y; t)$ ,  $\eta = \eta(x, y; t)$ , yields

$$\mathbf{J}^{-1} = \begin{bmatrix} \xi_x & \xi_y & \xi_t \\ \eta_x & \eta_y & \eta_t \\ \tau_x & \tau_y & \tau_t \end{bmatrix} = \frac{1}{J} \begin{bmatrix} y_\eta & -x_\eta & -(x_\tau y_\eta - y_\tau x_\eta) \\ -y_\xi & x_\xi & x_\tau y_\xi - y_\tau x_\xi \\ 0 & 0 & J \end{bmatrix},$$

so that the corresponding contravariant base vectors  $\mathbf{g}^1$ ,  $\mathbf{g}^2$ ,

$$\mathbf{g}^1 = \nabla\xi = [\xi_x, \xi_y] = [y_\eta, -x_\eta]/J, \quad \mathbf{g}^2 = \nabla\eta = [\eta_x, \eta_y] = [-y_\xi, x_\xi]/J, \quad (6)$$

$$\xi_t = -(x_\tau y_\eta - y_\tau x_\eta)/J, \quad \eta_t = (x_\tau y_\xi - y_\tau x_\xi)/J, \quad (7)$$

Therefore,  $\mathbf{v}_g = -(\xi_t \mathbf{g}_1 + \eta_t \mathbf{g}_2)$  is clearly obtained from Eqs. (4) and (7) with the definition of  $J$ . Now we have established the geometric relationship for our flow application.

By means of coordinate transformation, the equation of continuity in the general coordinate system is written, with fluid velocity  $\mathbf{u} = u^1 \mathbf{g}_1 + u^2 \mathbf{g}_2$ , by

$$\nabla \cdot \mathbf{u} = [(Ju^1)_\xi + (Ju^2)_\eta]/J = 0, \quad (8)$$

that defines the streamfunction by

$$u^1 = \psi_\eta/J, \quad u^2 = -\psi_\xi/J, \quad (9)$$

The Laplacian of  $\psi$  in Eq. (1) is easily derived, with replacing  $\mathbf{u}$  by  $\nabla\psi = (\psi_\xi \mathbf{g}^1 + \psi_\eta \mathbf{g}^2)$  in (8) through multiplying by  $\mathbf{g}^i$  ( $i = 1, 2$ ) to get the corresponding contravariant components of  $\nabla\psi$ ,

$$\nabla^2\psi = \nabla \cdot \nabla\psi = \left[ (Jg^{11}\psi_\xi + Jg^{12}\psi_\eta)_\xi + (Jg^{12}\psi_\xi + Jg^{22}\psi_\eta)_\eta \right] / J, \quad (10)$$

and the similar form for  $\nabla^2\omega$  in Eq. (2), where  $g^{ij} = \mathbf{g}^i \cdot \mathbf{g}^j$  for  $i, j = 1, 2$  are the contravariant metric tensors. In addition, through the chain rule, the material derivative of vorticity is transformed to

$$D\omega/Dt = \partial\omega/\partial t + \mathbf{u} \cdot \nabla\omega = \omega_\tau + U\omega_\xi + V\omega_\eta, \quad (11)$$

where the convective velocity of vorticity in this moving frame is equal to the flow velocity  $\mathbf{u} = u^1 \mathbf{g}_1 + u^2 \mathbf{g}_2$  relative to the grid velocity  $\mathbf{v}_g = -(\xi_t \mathbf{g}_1 + \eta_t \mathbf{g}_2)$ , written in contravariant components explicitly as

$$\begin{aligned} U &= u^1 + \xi_t = (\psi_\eta - x_\tau y_\eta + y_\tau x_\eta)/J, \\ V &= u^2 + \eta_t = (-\psi_\xi - y_\tau x_\xi + x_\tau y_\xi)/J. \end{aligned} \quad (12)$$

The drift effects on the fluid velocity due to the movement of grid point is thus clarified. Therefore, Eqs. (1) and (2) with (10)–(12) construct a general  $\psi$ - $\omega$  model to formulate the 2D unsteady viscous flow motion associated with the time-evolving irregular-grid geometry. The simple transformation by means of scalar formulation of  $\psi$  and  $\omega$ , instead of vectorial form in primitive variables  $\mathbf{u}$  and  $p$ , give us indeed the most favorable advantage in numerical practice when applied to a complicated moving boundary problem.

## 2.2. Initial conditions

The initial conditions are specified as the irrotational flow induced by a solitary wave of amplitude  $A_0$  with its peak at 15 times undisturbed water depths ahead of the cavity. The initial waveform ( $\zeta_f$ ) and celerity ( $C$ ) of a solitary wave are imposed by using the third-order approximate solutions of Grimshaw [6]

$$\begin{aligned} \zeta_f &= A_0 \cdot \operatorname{sech}^2 k \cdot \left[ 1 - \frac{3}{4} A_0 \cdot \tanh^2 k + A_0^2 \left( \frac{5}{8} \tanh^2 k \right. \right. \\ &\quad \left. \left. - \frac{101}{80} \operatorname{sech}^2 k \cdot \tanh^4 k \right) \right], \end{aligned} \quad (13)$$

$$C = 1 + \frac{1}{2} A_0 - \frac{3}{20} A_0^2 + \frac{3}{56} A_0^3, \quad (14)$$

in which  $k = \frac{\sqrt{3A}}{2} \left( 1 - \frac{5}{8} A_0 + \frac{71}{1280} A_0^2 \right) (x - X_0)$  and  $X_0$  = initial wave-peak position. The initial values of streamfunction at the free surface are given exactly as  $\psi_f = C\zeta_f$  while they are zero at other boundaries.

Meanwhile, the initial vorticity are zero in the whole flow region. Thus, under the irrotational flow assumption we calculate the streamfunction from Eq. (1) with the associated boundary conditions mentioned above in the flow domain as the desired initial conditions. Although Eqs. (13) and (14) are only the approximation

to the initial solitary wave solution, the real flow solution calculated in later time will be justified itself when we solve Eqs. (1) and (2) completely with the associated boundary conditions accurately.

## 2.3. Free surface boundary conditions

Here we neglect the vorticity generated by wave due to boundary layer being weak on the free-surface [18]. The effects of surface tension are also neglected since they are immaterial to the bottom vortical flow induced by a long wave. The dynamic condition on the free surface requires that the fluid pressure be atmospheric as a constant. From the transformed momentum equation with zero pressure gradient in the  $\xi$ -direction, the dynamic condition on the free surface  $y = \zeta(\xi, \eta_{\max}, \tau)$  becomes

$$Jg^{12}\psi_{\xi\tau} + Jg^{22}\psi_{\eta\tau} + \tilde{A}\psi_\xi + \tilde{B}\psi_\eta + (u - x_\tau)u_\xi + (\nu - \zeta_\tau)v_\xi + \zeta_\xi = 0, \quad (15)$$

where  $\tilde{A} = -(x_\eta/J)_\tau x_\xi - (\zeta_\eta/J)_\tau y_\xi$  and  $\tilde{B} = (x_\xi/J)_\tau x_\xi + (\zeta_\xi/J)_\tau y_\xi$  justify partially those temporal non-inertial effects of surface grid motion. As seen in Eq. (15), the first four terms relate to the relative local fluid acceleration and two subsequent terms containing  $u - x_\tau$  and  $\nu - \zeta_\tau$  are relative convective fluid acceleration represented in Cartesian coordinates while the last term  $\zeta_\xi$  represents the restoring gravitational force due to the free-surface elevation.

Besides the dynamic condition, we also need the free-surface kinematic condition that the normal component of relative fluid velocity to the free surface vanishes, i.e.,  $V = u^2 + \eta_t = 0$  in the second of Eq. (12), as in our previous discussion. This condition depicts the free surface  $y = \zeta(\xi, \eta_{\max}, \tau)$  as a material line by

$$\psi_\xi = \zeta_\tau x_\xi - x_\tau \zeta_\xi. \quad (16)$$

Using two boundary conditions (15) and (16), we can then solve for unknown  $\zeta$  and  $\psi$  on the free surface by iteration.

## 2.4. Bottom boundary conditions

The streamfunctions on a flat bottom and along the walls of cavity are specified as

$$\psi = 0, \quad (17)$$

which gives the zero tangential derivative of  $\psi$  along the wall. Meanwhile, the no-slip condition becomes

$$\psi_n = 0, \quad (18)$$

where the normal  $n$  to the wall is in either  $\xi$ - or  $\eta$ -direction as understood, and thus the definition of vorticity Eq. (1) gives the wall vorticity

$$\omega = -g^{nn}\psi_{nn}. \quad (19)$$

where  $g^{nn}$  is either  $g^{11}$  or  $g^{22}$ , depending on  $\psi_{nn}$  is either  $\psi_{\xi\xi}$  or  $\psi_{\eta\eta}$  accordingly. For the vorticity specified at corners of the cavity, we simply use zero vorticity conditions at the concave corners and use the average of vorticities, obtained as Eq. (19), respectively, from two outward normal directions, at the convex corners.

## 2.5. Open boundary conditions

The simple wave equations are applied to avoid the reflection of false waves from open boundaries, i.e.,

$$\theta_\tau \pm \sqrt{1 + \zeta}(\theta_\xi/x_\xi) = 0, \quad (20)$$

where  $\theta$  is a dummy variable representing either  $\psi$ ,  $\omega$  or  $\zeta$ . The upper sign in Eq. (20) is taken for the right boundary while the lower one for the left boundary.

### 3. Numerical schemes and grid system

#### 3.1. Finite analytic discretization formulation

No analytic solution could possibly be found when this flow is governed by the nonlinear system of equations with complicated boundary/initial conditions. However, the solution domain might be divided into many small elements or cells in which one can always linearize the governing equations locally and then solve them analytically at a satisfactory or tolerant accuracy. In this study, we utilize the Finite-Analytic (FA) method to discretize Eqs. (1) and (2), based on the local solution of a typical linearized 2D convection-diffusion transport equation (for  $\varphi$  denoting here either  $\psi$  or  $\omega$ )

$$\phi_{\xi^*\xi^*} + \phi_{\eta^*\eta^*} = 2A_\phi\phi_{\xi^*} + 2B_\phi\phi_{\eta^*} + S_\phi, \quad (21)$$

where the local coordinates are mapped by using  $d\xi^* = d\xi/\sqrt{g^{11}}$ ,  $d\eta^* = d\eta/\sqrt{g^{22}}$  with those linearized coefficients  $2A_\psi = -f^1/\sqrt{g^{11}}$ ,  $2B_\psi = -f^2/\sqrt{g^{22}}$ , or  $2A_\omega = (\text{Re}U - f^1)/\sqrt{g^{11}}$ ,  $2B_\omega = (\text{Re}V - f^1)/\sqrt{g^{22}}$ , and the source  $S_\psi = -2g^{11}\psi_{\xi^*\eta^*}/\sqrt{g^{11}g^{22}} - \omega$  or  $S_\omega = (\text{Re}(\omega - \omega^n)/\Delta\tau - 2g^{22}\omega_{\xi^*\eta^*}/\sqrt{g^{11}g^{22}})$ , all are frozen as constants evaluated at the elemental center  $P$ . We attach the superscripts  $n$  to the solution variable for the value at previous time step, but omit the superscripts  $(n+1)$  for those at the present time step. As noted, all these geometric coefficients are determined in the time-evolved grid system which is also a part of solution at the present time step. In practice, these frozen constants involved in Eq. (21) are updated within every time step until they are converged together with the flow variables.

By using the transformation

$$w = [\phi + S_\phi(A_\phi\xi^* + B_\phi\eta^*)/(2A_\phi^2 + 2B_\phi^2)] / \exp(A_\phi\xi^* + B_\phi\eta^*), \quad (22)$$

Eq. (21) becomes a homogeneous form

$$w_{\xi^*\xi^*} + w_{\eta^*\eta^*} = (A_\phi^2 + B_\phi^2)w, \quad (23)$$

whose general solutions inside the element  $|\xi^*| \leq \Delta\xi^*$ ,  $|\eta^*| \leq \Delta\eta^*$  can be obtained by the method of separation of variables in the Fourier eigenfunction expansion series

$$w = \left\{ \begin{array}{l} \sinh \mu_n \eta^* \\ \cosh \mu_n \eta^* \end{array} \right\} \left\{ \begin{array}{l} \sin \lambda_n \xi^* \\ \cos \lambda_n \xi^* \end{array} \right\} \text{ or } \left\{ \begin{array}{l} \sinh \mu'_n \xi^* \\ \cosh \mu'_n \xi^* \end{array} \right\} \left\{ \begin{array}{l} \sin \lambda'_n \eta^* \\ \cos \lambda'_n \eta^* \end{array} \right\},$$

associated with eigenvalues

$$\begin{aligned} \lambda_n \Delta \xi^* &= \lambda'_n \Delta \eta^* = n\pi/2, \quad \mu_n = \sqrt{A_\phi^2 + B_\phi^2 + \lambda_n^2}, \\ \mu'_n &= \sqrt{A_\phi^2 + B_\phi^2 + \lambda'_n^2}. \end{aligned}$$

Finally, the weighting coefficients (known as FA coefficients) of eigenfunctions are determined by Fourier transform of the continuous boundary conditions on the element. Chen and Chen [3] interpolated three boundary nodal values to obtain the continuous boundary condition on each side of the element. The interpolation formulation is similar to Patankar's exponential linear function [17] which is an exact solution of one-dimensional convection-diffusion transport equation. Other boundary formulations are referred to Chen and his research groups [4]. This treatment would give best physical senses on the rational process to discretize the flow Eq. (21).

Once these FA coefficients are obtained, the variable at the local center node  $\varphi_P$  is represented by weighted sum of discretized variables at eight neighboring (NB) nodes in the element and the weighted source as

$$\phi_P = \sum_{NB}^8 C_{NB} \phi_{NB} + C_P S_\phi. \quad (24)$$

where Chen and Chen [3] made the detailed derivation of the following formulas

$$C_E = E_B e^{-Ah}, \quad C_W = E_B e^{Ah}, \quad C_S = E_A e^{Bk}, \quad C_N = E_A e^{-Bk},$$

$$C_{NE} = E e^{-Ah-Bk}, \quad C_{NW} = E e^{Ah-Bk}, \quad C_{SE} = E e^{-Ah+Bk}, \quad C_{SW} = E e^{Ah+Bk},$$

$$C_P = \frac{1}{2(A^2 + B^2)} \left\{ Ah \tanh Ah + Bk \tanh Bk - 4 \cosh Ah \cosh Bk [(Ah)^2 E_1 + (Bk)^2 E_2] \right\},$$

$$E = \frac{1}{4 \cosh(Ah) \cosh(Bk)} - Ah E_1 \coth(Ah) - Bk E_2 \coth(Bk),$$

$$E_A = 2Ah \cosh(Ah) \coth(ah) E_1,$$

$$E_B = 2Bh \cosh(Bk) \coth(Bk) E_2,$$

$$E_1 = \sum_{m=1}^{\infty} \frac{-(-1)^m (\lambda_m h)}{[(Ah)^2 + (\lambda_m h)^2]^2 \cosh(\mu_m k)},$$

$$E_2 = \left( \frac{h}{k} \right) E_1 + \frac{Ak \tanh(Bk) - Bh \tanh(Ah)}{4AkBk \cosh(Bh) \cosh(Bk)},$$

$$\lambda_m = \sqrt{A^2 + B^2 + \mu_m^2}, \quad \mu_m = (2m-1)\pi/2/h, \quad m = 1, 2, 3, \dots, \infty.$$

The FA scheme possess a stable and accurate form of the most physical significance, just as discussed by Patankar [17] for the application of the one-dimensional heat flow of strong convection. This aspect is particularly useful on the present wave-induced vortical flow problem as well. Moreover, since the accuracy of local linearization and boundary-condition interpolation depends strongly on the grid size of the inner cell, the error control can thus be attainable through grid resolution analysis. This will be practically done to get a grid-independent solution by testing those numerical results in use of various grids.

As to the treatment of boundary conditions, we use the time-averaged finite difference (FD) scheme to deal with the nonlinear unsteady free-surface boundary conditions (15), (16), and the FD scheme for other boundary conditions for simplicity. Using these schemes in the solution process, we fully iterate all variables at every time step until they converge to satisfy all flow equations and boundary conditions. We set up the upper bounds of convergence at  $10^{-6}$  for both  $\psi$  and  $\zeta$ , and  $10^{-4}$  for  $\omega$ , according roughly to the order of magnitude of the variables on the applied grid size. We refer interested readers to the detailed numerical treatment and other flow examples in Tang and Chang [23,24]. Here only the grid system applied particularly in the present analysis is introduced.

#### 3.2. Base grid and overset grid refinement

It is certainly not practical to use a uniformly fine grid throughout the flow domain to get the accurate solution for the viscous, free-surface flow problems. Theoretical analyses and numerical experiments indicate that grid resolution is requested differently for the free-surface flow under wave motion and for the boundary layer flow near the solid boundary. Fine grid not only can resolve the great variation of solution variables in some region but also mimic nonlinear convection in justification for local linearization in FA formulation. Both can improve the solution accuracy. Therefore,

we construct an optimal hybrid grid system so that the global Base Grid (BG) is adopted for whole computational domain, with an Overset Grid (OG) for the refined region. The OG, as suggested here, is generated independently inside a small region like the local cavity region, without enforcing the overlap of BG and OG grid nodes at the interface. For convenience, we align both grids, however, only on the interface of OG and BG grid lines but not the overlap of grid nodes. This grid configuration will give us the most flexible control in OG resolution to analyze the local motion of vortices. In the present study, we concern with a very narrow flow region around the cavity, instead of a much larger wake region for transported vortices in Tang and Chang [23,24]. The OG is therefore designated the best for our present purpose.

To construct the desired BG system, the grid is first distributed evenly in both  $x$ - and  $y$ -direction beneath a rest free surface at initial instance. Then, as the free surface evolves with wave motion, we allow the upper half of the grid to move with time by redistributing the grid nodes evenly along every vertical gridline between the evolved free surface and the fixed lower boundary of this upper part. Thus, the horizontal  $x$ -coordinates of all grid nodes are kept stationary all the time and the  $y$ -coordinates of grid nodes can be changed only in the upper half part. The same methodology as BG construction can be utilized for OG generation, except for the uneven distribution of gridlines used by the latter. The uneven grid distribution is controlled by multiplying a constant ratio to expand the grid size from the densest grid lines, as shown in Fig. 3.

### 3.3. Overset grid system in the present application

As for an illustrated example, we use a square cavity of definite size  $W = D = 0.5$  ( $W$  = width and  $D$  = depth of cavity) to show how to generate the overset grid (OG) system to refine a local Base Grid (BG) region. Meanwhile, the efficiency of OG on the improved accuracy of flow solution can also be estimated. In the computational domain of  $-30 \leq x \leq 50$  and  $-1.5 \leq y \leq \zeta(x, t)$ , the BG of  $321 \times 31$  points (for the initial grid size about  $\Delta x = 0.25$ ,  $\Delta y = 0.05$ ) is employed in this study. When this BG system is applied to the calculation with the time interval of  $\Delta t = 0.1$  or  $0.05$ , the numerical result so obtained can provide us with a good basis to evaluate whether the accuracy of flow solution is improved as desired. Consider now a small region of width  $-3 \leq x \leq 3$  (about 7.5% of the global domain) consisting of the cavity to adopt the OG refinement throughout all water depth. For simplicity, we let all outer boundaries (i.e., two open boundaries at  $x = -3$  and  $+3$ , the free surface, and the flat bottom and cavity wall surface) of the OG region overlap with the BG lines and then obtain the

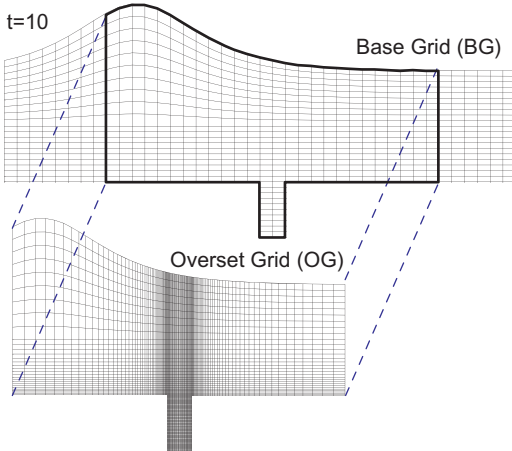


**Fig. 3.** Base Grid (BG) and Overset Grid (OG) applied at  $t = 10$  (for cavity  $W = D = 0.5$ , and solitary wave amplitude  $A_0 = 0.6$ ).

internal OG gridlines with the algorithm described before. In this refined region, we put  $424 \times 73$  grid points unevenly with the finest grid size  $\Delta_m = 0.01$  (defined as the minimum value of  $\Delta x$  and  $\Delta y$ ). However, a smaller amount of grid points will be used because those grid points on two sides of the cavity are outside the flow domain and we can remove them in actual calculations. Fig. 3 shows the instantaneous BG and OG around the cavity at  $t = 10$ , the time when a solitary wave of  $A_0 = 0.4$ , starting from  $X_0 = -15$  at  $t = 0$ , just enters the OG region.

Before solving the flow variables ( $\psi$ ,  $\omega$  and  $\zeta$ ) in the OG region, we first interpolate the lateral and upper (matching with the free surface) boundary values of these variables from the converged BG solution. Note that in this fine grid, the values of  $\psi$  and  $\omega$  at the solid boundary are treated exactly the same as those in the base grid. After interpolating the boundary values, we calculate the flow variables inside the domain through iterations until they are converged all together. Then, we will continue the computation for the next time step.

## 4. Results and discussion

### 4.1. Model validation for solitary-wave boundary layer flow on a flat bottom

Viscous effects on the damping of a solitary wave were discussed as early as by Russell in 1838, and then later by Keulegan [8], Ott and Sudan [16], Mei [15] and others. Recently, Liu and his colleagues (Liu and Orifici [13] and Liu et al. [14]) investigated, numerically and experimentally, the more detailed flow structure inside a laminar boundary layer on a flat bottom induced by the solitary wave. In this section, we follow Liu et al. [14] to study the laminar bottom boundary layer flow induced by a solitary wave. They applied PIV (particle image velocimetry) technique to measure the horizontal velocity profiles inside the bottom boundary layer in a water flume of undisturbed depth 10 cm. The typical Reynolds numbers in experiment were about  $10^5$  (based on the linear-long-wave celerity and the effective wavelength of solitary wave) for varied wave amplitudes 0.8, 2.0 and 3.0 cm. Since the action time is relative short for a solitary wave passing by a fixed point on the bottom, it requires much higher value of Re for an unsteady flow to induce the fluid from its initial rest state to develop turbulence. More experimental evidences were discussed by Sumer et al. [21]. We will only make laminar flow analysis here.

Fig. 4 compares the calculated horizontal velocity profiles from the present  $\psi-\omega$  model with Liu's measured data and their numer-

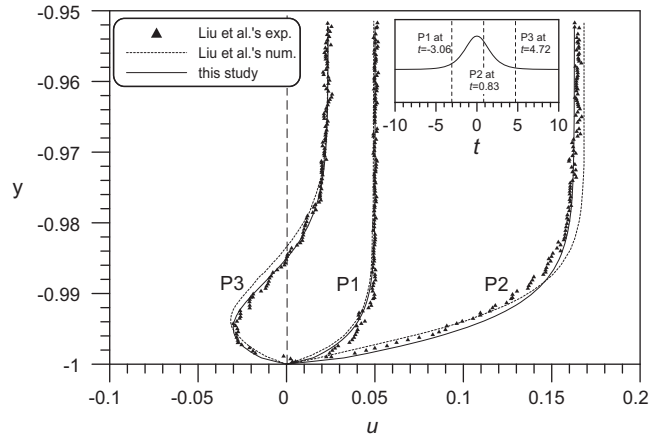


**Fig. 4.** Comparison of three horizontal velocity profiles in the flat-bottom boundary layer (for Reynolds number  $Re \approx 10^5$  and amplitude  $A_0 = 0.2$ ).

ical result at three different phases. The velocity profile of the finest grid space  $\Delta_m = 0.001$  is considered to reveal at closer to the bottom in the boundary layer in this case. The excellent agreement among these results is shown. The accuracy of flow solution within a thin boundary layer, together with the permanent waveform property of solitary wave (tested in Tang and Chang [23,24], by the present flow model is thus validated. In Liu's numerical work, they obtained the consistent numerical solutions for both linear and nonlinear boundary layer flow equations. Particular for linear

boundary layer calculation, they used the kernel function of diffusion equation with distributed source strength of specified bottom slip velocity (i.e., the solitary-wave solution of Grimshaw's). This approach is actually equivalent to the one suggested by Lighthill ([12], on page 58), using a Gaussian distribution of vorticity source generated stepwise by slip velocity increment on wall. Both approaches in the local analysis implicitly support that the global usage of  $\psi-\omega$  model in the whole field is an effective way to involve the consistent physical features.

The appearance of reversed flow inside the boundary layer near the flat bottom with zero bottom shear stress at some point on the bottom, with the decelerated free stream in the outer region, is one instance of vagueness to us whether the flow is separated or attached, because the boundary layer solution does not supply us with enough information to make this judgment, unless further investigation on the flow pattern is carried out. Fig. 5 gives the global flow pattern represented by the detailed streamline contour around the point of zero bottom shear stress or zero bottom vorticity in the magnified draw. We plot the streamline pattern intentionally by two various intervals of contour level, one range by increment  $\psi = 0.005$  within  $\psi = 0-0.215$  (the maximum that appears right under the wave crest) and the other by finer increment  $\psi = 0.001$  for negative  $\psi$ -value. From this figure, we clearly observe that the limiting streamline indeed attaches the bottom surface in the deceleration phase behind the crest of the solitary wave. Thus, the global flow analysis, especially illustrated by the correspondent streamline distribution, gives much comprehensive physical description over the local analysis.

In the following, we will consider the cavity flow with varied  $W$ ,  $D$  (width and depth of the cavity) and  $A_0$  (initial solitary wave amplitude) and compare their effects on the flow field. Although more calculations are carried out for varieties of  $W$ ,  $D$  and  $A_0$  in

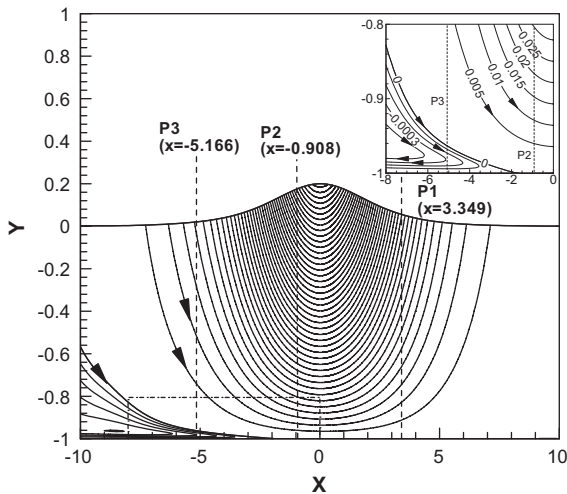


**Fig. 5.** Global and local streamline contours under a solitary wave  $A_0 = 0.2$  in motion (contour levels:  $\Delta\psi = 0.005$  for  $\psi > 0$ , and  $\Delta\psi = 0.001$  for  $\psi < 0$ ).

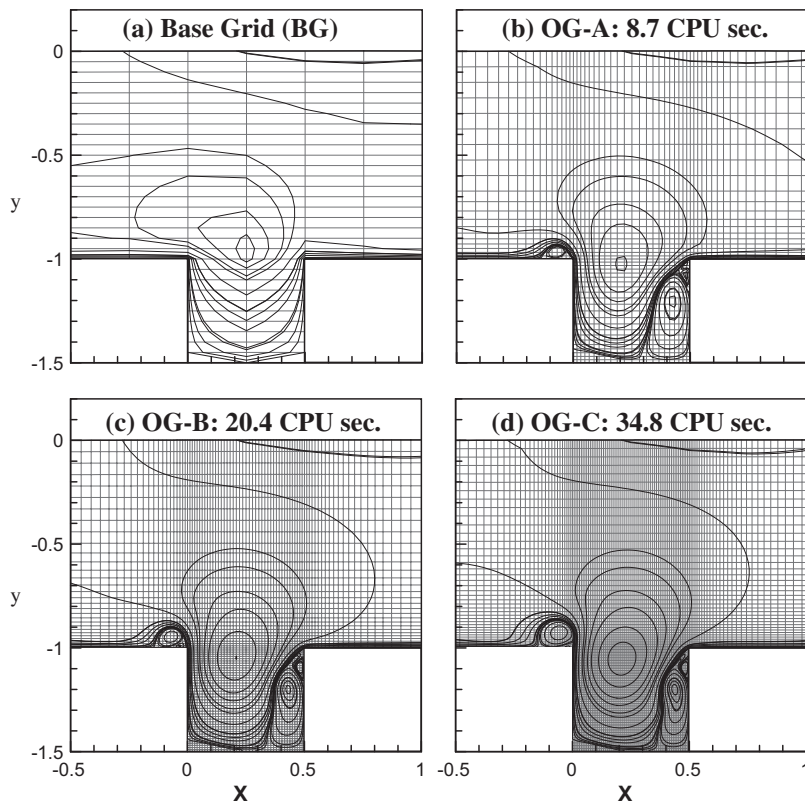


**Fig. 6.** Streamlines by using various grids: (a) BG; (b) OG-A; (c) OG-B; (d) OG-C at  $t = 20$  for  $W = D = 0.5$  and  $A_0 = 0.6$ ; CPU sec's shown the times required for one time step calculation).

our analysis, only partial results of the evolved free-surface and the corresponding vortical flow pattern will be discussed here. Among them, the flow for  $W = D = 0.5$  and  $A_0 = 0.4$  is considered as the typical flow case, if not mentioned specifically in the article. Besides, the initial peak position of the incident solitary wave is always set at  $X_0 = -15$ , in contrast to the upstream face of the cavity situated at  $x = 0$ . We may thus expect the wave passing through the cavity around the time  $t = 12\text{--}14$ , depending on its celerity or wave amplitude as in Eq. (14).

#### 4.2. Assessment of overset grids in cavity flow solution

We consider in this section the influence of OG system on the accuracy of flow solution and its computational efficiency to obtain the solution. Conventionally, the numerical solutions using different grid resolutions for a specific grid system are usually compared with each other to find out a solution of the least influence of the applied grid. We can also track information of numerical performance like convergent rate, computing time, etc. through these comparisons. The overall comparison can confide in the reliability and efficiency of numerical model in some senses, in addition to the discretization and matrix iteration processes.

**Fig. 6** shows the streamline contours of four flow solutions by using various grids at  $t = 20$ . The improvement of flow solution obtained from the BG system in **Fig. 6a** is seen by those from three OG systems of various grid resolutions,  $384 \times 43$  (for OG-A),  $424 \times 73$  (for OG-B), and  $464 \times 103$  (for OG-C), respectively, as shown in **Fig. 6b-d**. Among these three grids, the smallest grid sizes  $\Delta_m$  are 0.015 (for OG-A), 0.01 (for OG-B), and 0.005 (for OG-C), respectively. The use of finest grid (OG-C) in calculation should reasonably give the relative more accurate result, according to our previous numerical experiment. The predicted flow patterns from OG-B and OG-C calculations are found almost the same in most of characteristic features, even for those small-scaled vortices near cavity corners. We also show the required computing time (in CPU seconds required for completing one time step calculation to get a converged solution) for three OG systems in **Fig. 6**. In all our calculations we use a personal computer with an Intel Pentium IV 2.6 GB CPU, as known an old desktop computer of limited memory, to estimate the required CPU time. For a total of 200 time steps ( $t = 20$  with  $\Delta t = 0.1$ ), the calculation using the OG-A system takes less than 30 minutes long to finish the task while OG-B takes about one hour and OG-C takes about 2 hours, counting for the typical time shown in **Fig. 6**. To compromise on overall performance, we believe that the use of OG-B was more favorable in consideration of both solution accuracy and numerical efficiency. Thus, this

OG-B system will be utilized in all our later calculations for cavity flow without further mention.

To make further the quantitative assessment among three grid systems, we analyze the minimum values of instantaneous streamfunction ( $\psi_{\min}$ ) taken right at the core of primary vortex A. Because the limiting streamline enclosing a vortex is identified to be the zero value of  $\psi$ , the instantaneous value of  $\psi_{\min}(t)$  could represent approximately for the circulating flow flux by a vortex of evolved strength and size. For the evolved size, it has been analyzed as the flow pattern in **Fig. 6**. For the evolved strength of the primary vortex A, **Fig. 7** indicated the evolution of circulation  $\Gamma(t)$  and the core streamfunction value  $|\psi_{\min}(t)|$ , corresponding to numerical results obtained respectively from three OG systems. Between the two evolutions, the core value of streamfunction is much easier to obtain simply by searching its minimum value inside the entire flow field. On the other hand, circulation must be evaluated along a closed loop C around an isolate vortex, which is defined by

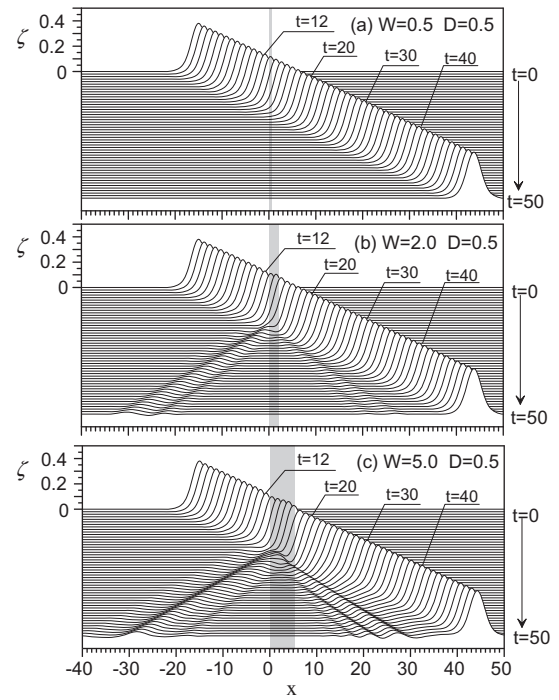


**Fig. 8.** Evolved wave profiles, plotted per unit time interval up to  $t = 50$ , across a cavity (shades) of varied widths (for  $D = 0.5$  and  $A_0 = 0.4$ ).

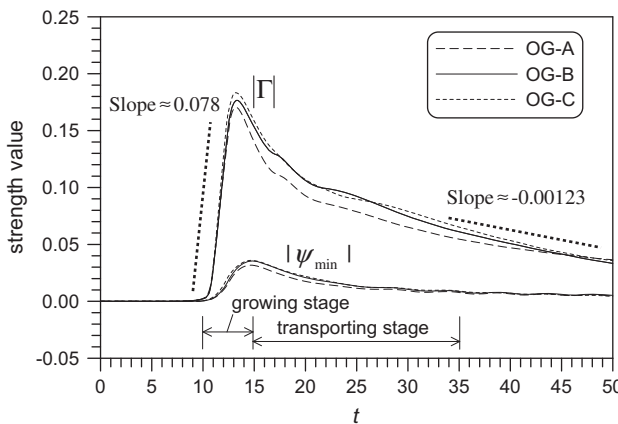


**Fig. 7.** Evolved circulation and minimum of streamfunction at the core of primary vortex (for  $W = D = 0.5$  and  $A_0 = 0.6$ ).

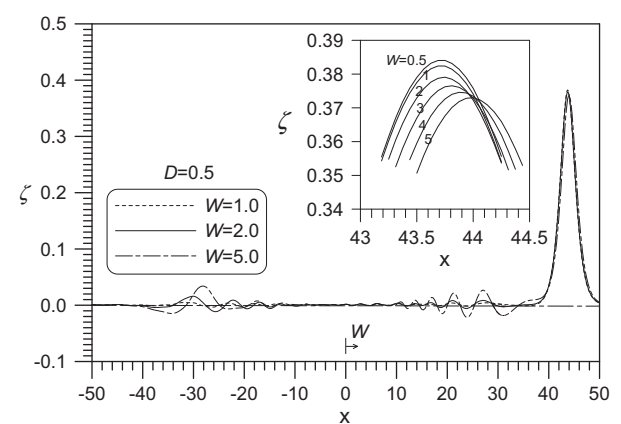


**Fig. 9.** Effects of cavity width on wave profiles and crests at  $t = 50$  (for  $D = 0.5$  and  $A_0 = 0.4$ ).

$$\Gamma \equiv \oint_C \vec{u} \cdot \vec{t} ds, \quad (25)$$

in which  $\vec{u}$  is the velocity vector and  $\vec{t}$  is a unit vector tangent to the curve. Using Stokes' theorem, we can transform the line integral to a regional integral in the curvilinear coordinates and approximate it by the discrete form within the region

$$\Gamma = \int \int_A \omega dA = \int \int_A \omega J dd\xi d\eta \approx \sum_{\text{inside vortex}} (\omega J)_{ij}, \quad (26)$$

where the second-order trapezoidal quadrature rule is applied with  $d\xi = d\eta = 1$ , and  $\omega = 0$  on the outer boundary of the vortex. Thus, we can estimate the local strength of an isolate vortex by  $\Gamma(t)$  in the typical way to quantify a circular vortex evolved with time. As seen from Fig. 7, three time stages, say, the formation, transport, and de-

cay of the primary vortex during evolution can be clearly identified. In the first stage of vortex formation, we find out that the circulation of the primary vortex grow its strength quickly, at a constant rate of 0.0789, up to a peak value of 0.18 at about  $t = 14.6$  when the solitary wave crest right reaches above the cavity. However, the peak value of  $|\psi_{\min}| = 0.035$  is found a little delay at  $t = 14.8$ , instead. Then, in the deceleration phase, the vortex begins to decrease with time at varied rates of decay, from faster to slower, in the transport stage. The enhancement of new vortex strength in the opposite sense cancels out the previous vortex sheet created in the acceleration phase. Finally, its decay slowly by viscous diffusion reaches at a constant rate of 0.00213. More numerical features in Fig. 7 also give some quantitative insights on evaluation of solution accuracy among using these three grids. The well agreed result between using OG-B and OG-C systems again confirms the solutions well along with time.

#### 4.3. Free-surface evolutions in cavity flow

Consider the influence of a cavity of varied sizes on the free-surface elevation for the solitary wave of initial wave height  $A_0 = 0.4$ . We plot the evolved free-surface profiles, at intervals of two time

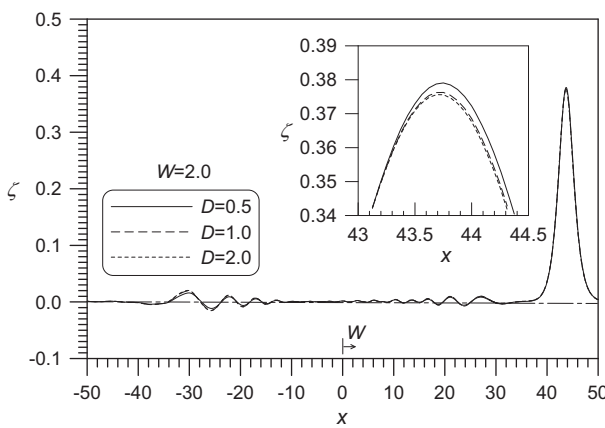


**Fig. 10.** Effects of cavity depth on wave profiles and crests at  $t = 50$  (for  $W = 2$  and  $A_0 = 0.4$ ).

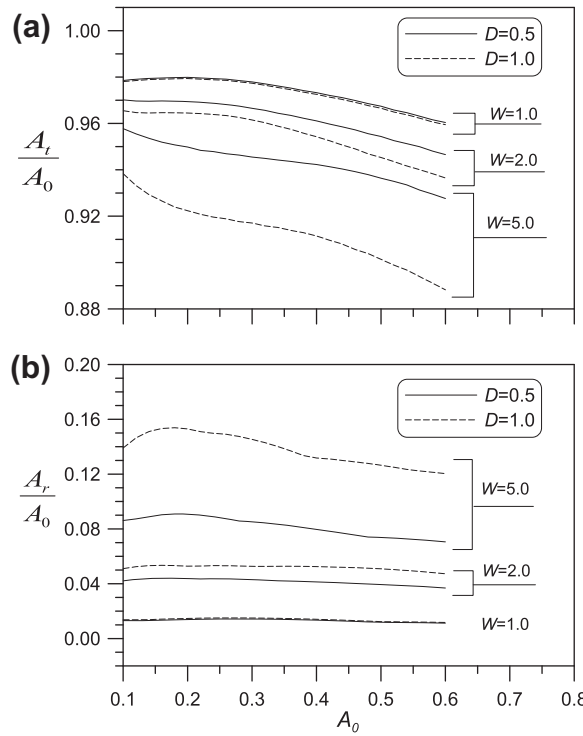


**Fig. 11.** Incident wave height versus wave amplitude ratios for (a) transmission ( $A_t/A_0$ ), and (b) reflection ( $A_r/A_0$ ) coefficients.

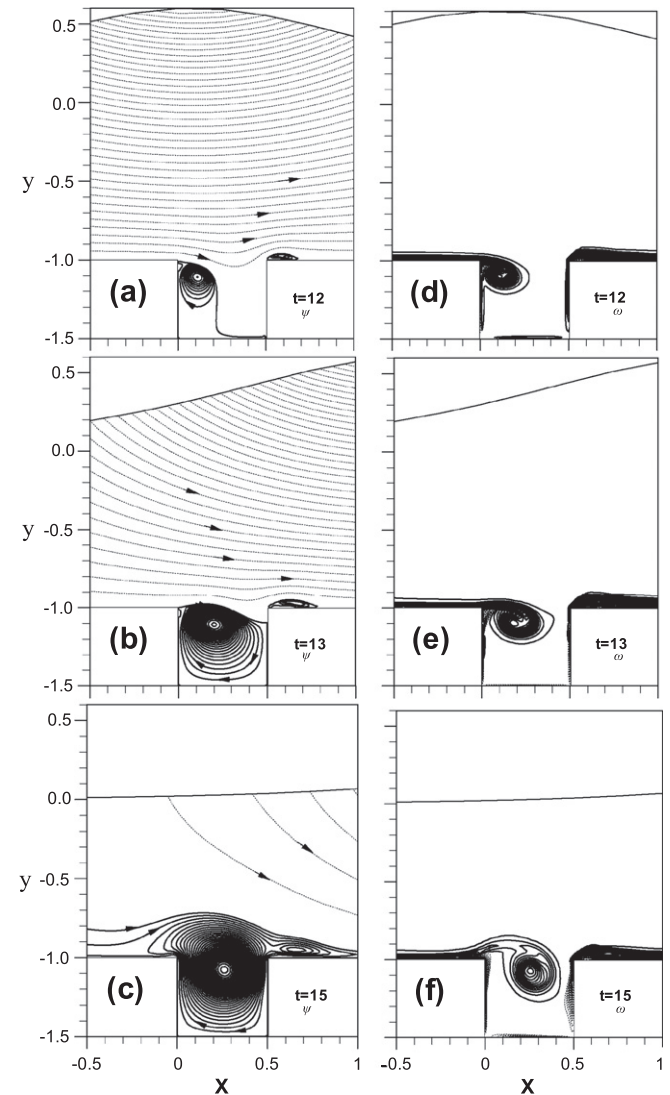


**Fig. 12.**  $\psi$ - $\omega$  Distributions at vortex generation stage  $t = 12, 13$  and  $15$  (for  $D = W = 0.5$  and  $A_0 = 0.6$ ). Contour levels:  $\Delta\psi = 0.02$  for  $\psi > 0$  (dash), and  $\Delta\psi = 0.001$  for  $\psi < 0$  (solid);  $\Delta\omega = 0.4$  for both  $\omega > 0$  (dash) and  $\omega < 0$  (solid).

units until  $t = 50$ , in Fig. 8a–c as this wave passes through a cavity of varied widths  $W = 0.5, 2$  and  $5$ , respectively, and a fixed depth  $D = 0.5$ . In addition, the shading strips in these figures indicate the location and width of the cavity. Specific free-surface profiles are marked with time so that we can easily locate the instantaneous position of the solitary wave peak and estimate the effective region of flow induction through the wave motion. From the perspective view of wave crest or trough lines in Fig. 8, trains of the reflected waves and the transmitted tail waves can be clearly seen, for instance, in Fig. 8b, but oppositely are not detectable in Fig. 8a. This means that the cavity width of  $0.5$  (water depth) is too small to affect the wave of large wavelength like a solitary wave while the wider a cavity is, the larger the disturbance scatters for both the reflected waves and the transmitted tail waves. It indeed becomes more significant to disperse the scattering waves for  $W = 5$  in our calculation.

In Fig. 9, we plot the free-surface elevation of transmitted and reflected waves evolved at  $t = 50$  when a solitary wave of initial amplitude  $A_0 = 0.4$  run cross the cavity of  $D = 0.5$ . The wave profiles

near the wave crest are also amplified in a small box in Fig. 9 to illustrate the effects of the cavity width on the crest. For a wider cavity the transmitted wave is lower, but the amplitude of trailing waves and reflected waves are higher. It is clear the energy is dissipated when the wave advancing across the cavity to attenuate its transmission. The influences of depth on the waveform are generally less than those of width, which are shown in Fig. 10. Fig. 10 compares the influence of various cavity depths  $D = 0.5, 1.0$ , and  $2.0$  on the wave elevation with the constant width of cavity,  $W = 2.0$ . From the amplified plot near the wave crest, we see the waveform near the crest becomes less affected by the depth when  $D > 1$ . The trailing wave following the main wave and its reflected wave appears in almost the same pattern at this width of cavity. As mentioned before, the width and depth of cavity will influence the transmitted and reflected waves. The transmitted coefficients ( $A_t/A_0$ ) and reflected coefficients ( $A_r/A_0$ ) for various  $A_0$  are plotted in Fig. 11 with respect of the three widths ( $W = 1.0, 2.0$ , and  $5.0$ ) and the two different depths ( $D = 0.5$  and  $1.0$ ). It illustrates for wider width the depth effect is stronger resulting in the smaller

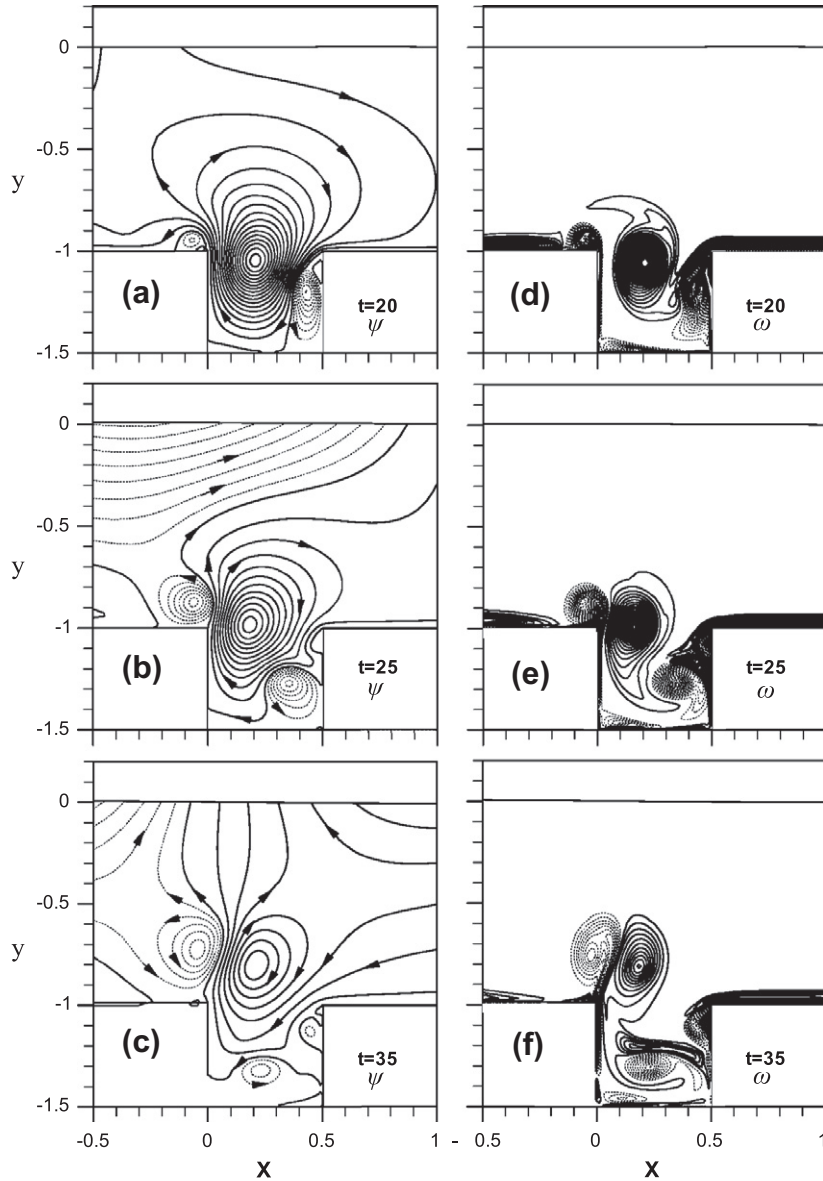


**Fig. 13.**  $\psi$ - $\omega$  Distributions at vortex transportation stage  $t = 20, 25, 35$  (for  $D = W = 0.5$  and  $A_0 = 0.6$ ). Contour levels:  $\Delta\psi = 0.0005$  for  $\psi > 0$  (dash), and  $\Delta\psi = 0.001$  for  $\psi < 0$  (solid);  $\Delta\omega = 0.1$  for both  $\omega > 0$  (dash) and  $\omega < 0$  (solid).

transmitted waves but larger reflected waves. It is interesting to note the values of reflected coefficient for the different  $D$  with same  $W$  are almost independent of  $A_0$ .

#### 4.4. Vortical flow patterns in cavity flow

We investigate the evolved vortical flow pattern for  $A_0 = 0.6$  and  $W = D = 0.5$  at three different time stages, according to the generation and evolution of vortices during the transport process. Among them, we identify the first stage for the initial vortex generated by the wave-induced flow, then observe the convective and diffusive transport of developing vortices at the second stage, and at the last stage for the viscous diffusion of the well-developed vortices. In our discussion, we correspond three selected durations, namely,  $12 \leq t \leq 15$ ,  $20 \leq t \leq 35$  and  $t = 50$  to demonstrate these three time stages.

##### 4.4.1. Stage I: initial generation of vortices

In this time stage ( $12 \leq t \leq 15$ ), the solitary wave is just passing by the cavity to induce the local separated flow to generate the

vorticity in the boundary layers along the bottom surface and to transport it inside of the cavity. Initially, the induced flow has two separation points right at two top corners of cavity. At the front separation point, the induced flow is forced to separate immediately from the leading top edge of cavity and reattach to the front vertical wall inside the cavity. Meanwhile, it also separates immediately at the rear edge behind the cavity and reattaches to the downstream bottom surface. However, the rear circulating zone is much smaller in size. As time increases, the outer wave-induced flow accelerates before the wavepeak gets to the cavity, and decelerates afterward. We can consult Fig. 8, or use Eq. (14) for estimation of the arrival time (about  $t = 12\text{--}13$ ) of wave peak to reach the cavity. As generated on the solid wall by viscous friction, the vorticity is transported downstream by convective and viscous diffusion. As a result, the concentrated vorticity forms an isolated vortex with concentric streamlines around its core.

At this initial stage, we plot the streamline contours in the left column or Fig. 12a–c and the corresponding vorticity contours in Fig. 12d–f, respectively, at  $t = 12$ ,  $13$  and  $15$  for  $A_0 = 0.6$ . The three free surfaces shown on this figure illustrate the crude information

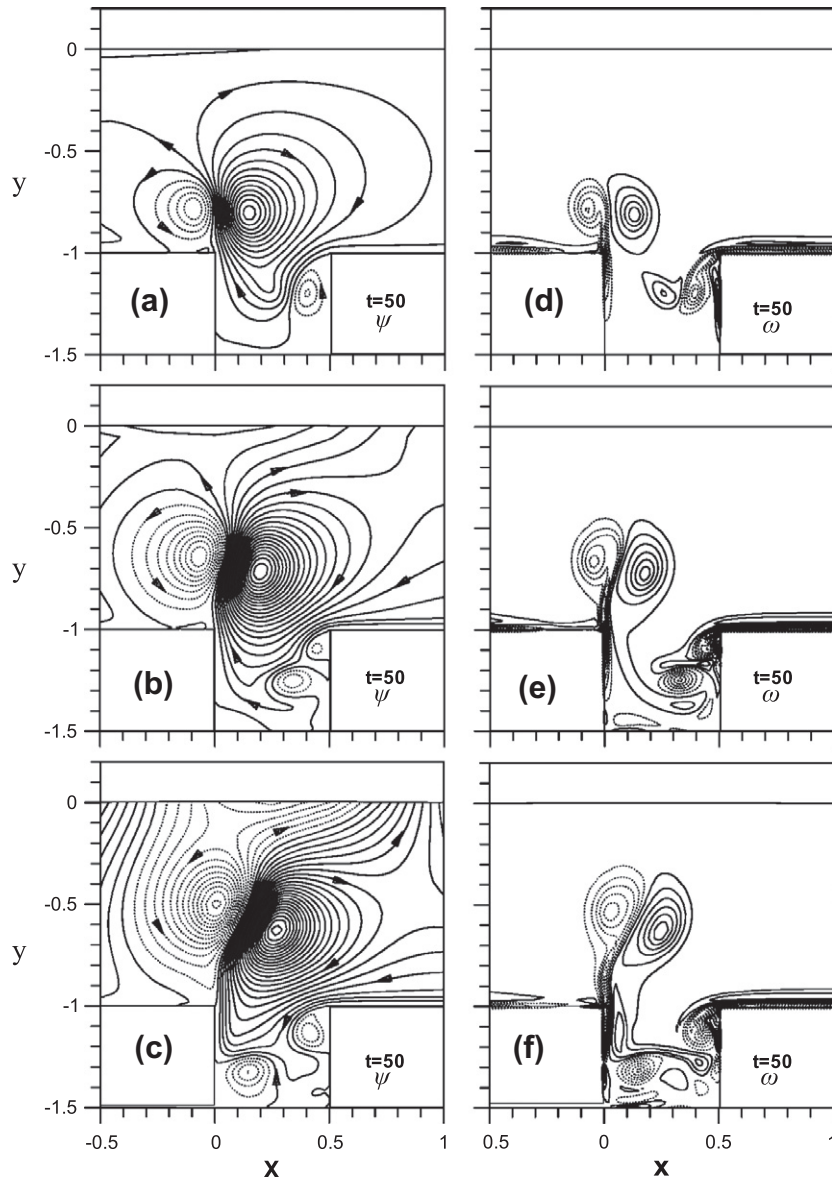


**Fig. 14.**  $\psi$ - $\omega$  Distributions at  $t = 50$  around a cavity ( $W = D = 0.5$ ) for wave amplitudes  $A_0 =$  (a) 0.2, (b) 0.4, (c) 0.6. Contour levels:  $\Delta\psi = 0.0002$ ,  $\Delta\omega = 0.1$  for both positive (dash) and negative values (solid).

of corresponding wave motion while the streamlines and vorticity distribution beneath the free surfaces describe the induced flow in more detail. In order to detect the slow wave-induced flow motion near the bottom and cavity, we plot intensive contour lines between small range of 0.02 to  $-0.02$  at interval of 0.001, instead of 0.02, beyond this range. It should be recalled that the bottom and cavity walls always have the zero value of  $\psi$ . Fig. 12a shows two vortices generated from the separated flow at  $t = 12$ , in which, as marked in Fig. 1, vortex A inside the cavity is from the left top corner of cavity while vortex D outside the cavity occurs on the bottom behind the right corner. Fig. 12d gives the information on where those concentrated vorticity bulbs are. As time preceeds, vortex A grows with increasing its strength and migrates its core to the center of cavity at  $t = 13$  (Fig. 12b and e). However, the outer flow restricts the vorticity diffusion inside the cavity. When  $t = 15$ , as seen in Fig. 12c and f, the outer flow finally becomes weaker (owing to dilute streamlines) and the upper part of vortex A extends itself outside of the cavity, although the vortex core is still inside of the cavity.

#### 4.4.2. Stage II: transport of developing vortices

From this stage ( $15 \leq t \leq 35$ ), there is a very weak outer flow induced by the scattered wave train. Similarly, Fig. 13 shows the streamlines contours (in Fig. 13a–c) and vorticity distribution (in Fig. 13d–f) during  $t = 20, 25$  and  $35$ , the time during which the vortices are developing themselves around the cavity region. At  $t = 20$  (Fig. 13a and d), the upper part of primary vortex A diffuses quickly upward, as compared to their counter-plots in Fig. 12c and f, and its core begins to migrate outside of the cavity. On the left of vortex A, the counter vortex B is also developed in Fig. 13a and d. Later ( $t = 25$ , and  $35$ ), the pair of vortices A and B are convected together upward to form a jet to emanate fluids from the cavity. On the other hand, vortex C, standing aside on the right of vortex A at

$t = 20$ , inserts into the bottom of vortex A to lift it out of the cavity, as seen at later time  $t = 25$  and  $t = 35$ . During this period, a new group of vortices (still named as vortices D for simplicity) develops in the rear edge of the cavity and grows slightly between  $t = 25$  and  $35$ . More interesting, reflection mechanism makes the local reversed flow around vortices D driving the downstream fluid from the bottom surface backward into the cavity, as seen in Fig. 13a–c, with all the equi-vorticity lines parallel to the downstream bottom in Fig. 13d–f.

#### 4.4.3. Stage III: diffusion of developed vortices

In the final stage, the core of vortices becomes stationary with slow diffusion due to viscosity, as shown in Fig. 14c and f. In addition to the vortical flow pattern for  $A_0 = 0.6$  that has been completely studied in previous time stages, we exam the weaker flow patterns for  $A_0 = 0.2$  and  $0.4$  at this fully-developed stage. Fig. 14 presents these three flow patterns developed at  $t = 50$ . In Fig. 14d, the weak solitary wave ( $A_0 = 0.2$ ) induces two pairs of vortices, namely, the parent pair A–B in the upper front of and the daughter pair C–D on the backward face of the cavity. In contrast to  $A_0 = 0.2$ , the largest solitary wave of  $A_0 = 0.6$  induce a more complicated flow pattern with several vortex pairs around the cavity, as seen in Fig. 14f. This makes picturesque contrast of distinguished features among the developed flow patterns influenced by three  $A_0$ 's.

We can also compare the combined effects of cavity's width and depth on the developed vortex pattern. We consider the cavity of depth  $D = 1$ , twice of all previous discussed cases for three various widths of  $W = 0.5, 1$  and  $2$  in Fig. 15. As the cavity becomes wider, two pairs of vortices A–B and C–D leaves farther away from each other. For wider width, both pairs of vortices are developed independently without interaction. Notice that Fig. 15a and d has the same width ( $W = 0.5$ ) as Fig. 14c and f, but of different depths.

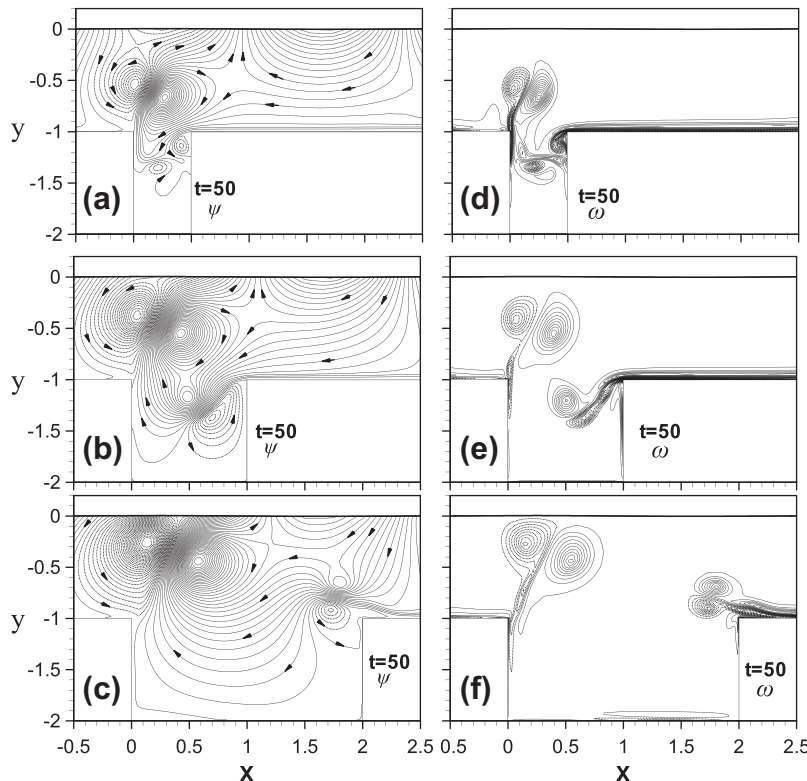


**Fig. 15.**  $\psi$ – $\omega$  Distributions at  $t = 50$  for a cavity of varied widths  $W =$  (a) 0.5, (b) 1, (c) 2 ( $D = 1$  and  $A_0 = 0.6$ ). Contour levels:  $\Delta\psi = 0.0002$ ,  $\Delta\omega = 0.05$  for both positive (dash) and negative values (solid).

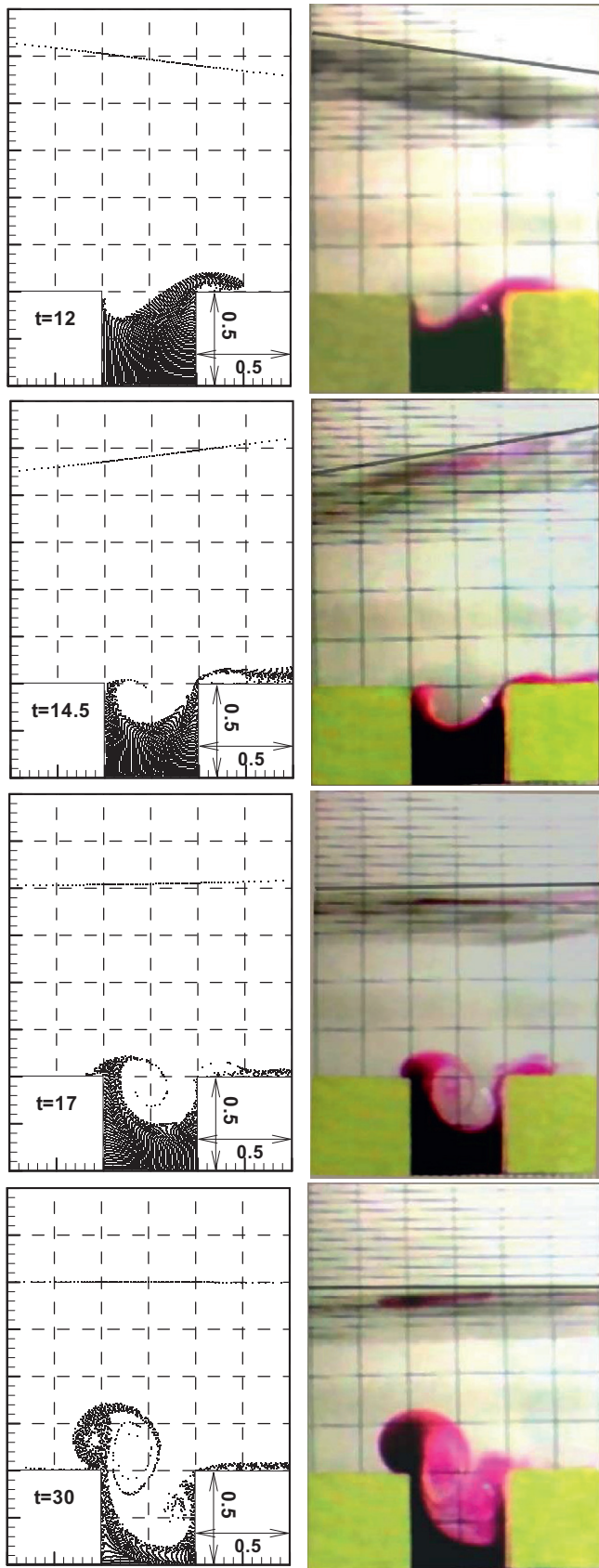


**Fig. 16.** Particle motions for a solitary wave with  $A_0 \approx 0.35$  passing over a cavity: numerical simulation (left) and experimental observation (right).

The vortex patterns between both have little differences in structure, which implies the limiting effects of depth on the developed

vortices for this width. It is expected that the depth effects will probably be essential for a wider cavity under the action of a long wave. However, as the width of a cavity increases, the interaction among wave and structure becomes stronger at the same time. The wave dispersion scattered by a wider cavity not only affects significantly the wave deformation, on the primary wave height together with the reflected and the transmitted trail waves, but also influences the local vortical flow pattern around the cavity. The interesting wave–flow–vortices interaction problems for a solitary wave passing by an extremely wide valley or even the backward-forward step are another important issue but not concerned here.

Qualitative comparisons of the simulated particle motions were also made with dye visualization on another tested model in a smaller water flume, much like the one mentioned previously. This experiment improves the previous setup (obtain the results of Fig. 2) by keeping the model cavity embedded below the flat bottom of the flume. The solitary wave was simply generated by pushing a vertical plate on a carriage for a small distance by hand, still without checking whether its waveform is consistent with Grimshaw's waveform (Eq. (13)) because we were more concerned with the vortex evolution. The flow motion and the free surface elevation are recorded directly by a video camera. In the numerical work, 2500 fluid particles are virtually filled evenly in the cavity at  $t = 0$  and traced later in the Lagrangian sense. Fig. 16 shows the comparison of particle motion between the simulated result and the experimental visualization for an incident wave of approximate height  $A_0 = 0.35$  and  $Re = 25,000$ . The agreement of both results in their evolved flow patterns is quite well.

The study on the removal of particles can as well light on some practical issues concerning the ocean environmental ecology. Through this wave–flow interaction mechanism, the induced vortical flow can activate and transport sediments, nutrition or plankton from bottom irregularities like cavities into the open ocean environment. It is therefore worthy to study the stratified particle motion extensively and carry out more cautious experiments in the future.

## 5. Conclusions

This paper applied the numerical method to simulate the vortex generation and its consequent evolution in the tranquil ambience when a solitary wave passes over a cavity on the shallow water bottom. A streamfunction–vorticity model was treated in a boundary-fitted grid system with the refinement of using Overset Grid (OG). In addition, the hybrid discretization scheme of FA and FD method was introduced. These enable to seek a converged and accurate solution to satisfy the flow equations and associated boundary conditions at every time step. With grid refinement, we indeed not only improve solution accuracy but also obtain computation economics.

The boundary layer flow on the flat bottom caused by a solitary wave propagating along a uniform channel was simulated and used to validate the numerical model in this study. Then, the effects of cavity size and incident wave amplitude on the vortical flow pattern and the free surface elevation were studied. The numerical results show the cavity width of 0.5 (water depth) is too small to affect the wave of large wavelength like a solitary wave while the wider a cavity is, the larger the disturbance scatters for both the reflected waves and the transmitted tail waves. It indeed becomes more significant to disperse the scattering waves for the larger width ( $W = 5$ ) in our calculation. In the part of wave transformation, for wider width the depth effect is stronger resulting in the smaller transmitted waves but larger reflected waves. Also, it is found the values of reflected coefficient for the different  $D$  with same  $W$  are almost independent of  $A_0$ . For the vortical flow

in cavity, three stages of vortex motion are clarified in sequence: (I) generation and growth, (II) transportation and (III) jet formation.

In short, this paper includes the free surface evolutions with time and the mechanism of vortex generation and transportation around the cavity. The consistent agreement of flow patterns between numerical and experimental results was demonstrated.

## Acknowledgements

This study sponsored by NSC96-2221-E-275-003 in Taiwan is acknowledged. Special thanks to Prof. Yee-Chung Jin for helpful comments.

## References

- [1] Chang K, Constantinescu G, Park S. Analysis of the flow and mass transfer processes for the incompressible flow past an open cavity with a laminar and a fully turbulent incoming boundary layer. *J Fluid Mech* 2006;561:113–45.
- [2] Chang K-A, Hsu T-J, Liu PL-F. Vortex generation and evolution in water waves propagating over a submerged rectangular obstacle: Part I. Solitary waves. *Coas Eng* 2001;44(1):13–36.
- [3] Chen CJ, Chen HC. Finite analytic numerical method for unsteady two-dimensional Navier–Stokes equations. *J Comp Phys* 1984;53:209–26.
- [4] Chen CJ. The finite analytic method, vol. 232. Iowa Institute of Hydraulic Research, U Iowa, Iowa City, IIHR report; 1982. p. 1–8.
- [5] Gresho PM. Incompressible fluid dynamics: some fundamental formulation issues. *Ann Rev Fluid Mech* 1991;23:413–53.
- [6] Grimshaw R. The solitary wave in water of variable depth. Part 2. *J Fluid Mech* 1971;46(3):611–22.
- [7] Hsu TW, Hsieh CM, Hwang RR. Using RANS to simulate vortex generation and dissipation around impermeable submerged double breakwaters. *Coast Eng* 2004;51:557–79.
- [8] Keulegan GH. Gradual damping of solitary wave. *J Res Natl Bur Stand* 1948;40:607–14.
- [9] Lin C, Ho T-C, Chang S-C, Hsieh S-C, Chang K-A. Vortex shedding induced by a solitary wave propagating over a submerged vertical plate. *Int J Heat Fluid Flow* 2005;26:894–904.
- [10] Lin C, Ho TC, Chang SC, Chang KA. Laboratory observation of a solitary wave propagation over a submerged rectangular dike. *J Engrg Mech* 2006;132(5):545–54.
- [11] Lin P. A numerical study of solitary wave interaction with rectangular obstacles. *Coast Eng* 2004;51(1):35–51.
- [12] Lighthill MJ. Boundary layer theory II. Introduction laminar boundary layers. Ed Rosenhead L, Oxford Univ Press; 1963.
- [13] Liu PL-F, Orifilia A. Viscous effects on transient long-wave propagation. *J Fluid Mech* 2004;520:83–92.
- [14] Liu PL-F, Park YS, Cowen ES. Boundary layer flow and bed shear stress under a solitary wave. *J Fluid Mech* 2007;574:449–63.
- [15] Mei CC. Theory and applications of ocean surface waves, vol. 2. World Scientific; 2005.
- [16] Ott E, Sudan RN. Damping of solitary waves. *Phys Fluids* 1970;13(6):1432–4.
- [17] Patankar SV. Numerical heat transfer and fluid flow. McGraw-Hill; 1980.
- [18] Patel VC, Landweber L, Tang CJ. Free-surface boundary layer and the origin of bow vortices. In: Second Inter Sym Ship Viscous Resistance. Göteborg, Sweden; 1985. p. 23:1–13.
- [19] Rowley CW, Williams DR. Dynamics and control of high-Reynolds-number flow over open cavities. *Ann Rev Fluid Mech* 2006;38:251–76.
- [20] Shankar PN, Deshpande MD. Fluid mechanics in the driven cavity. *Ann Rev Fluid Mech* 2000;32:93–136.
- [21] Sumer BM, Jensen PM, Sørensen LB, Fredsøe J, Liu PL-F. Turbulent Solitary Wave Boundary Layer. In: Proc 18th Int Offshore Polar Eng Conference, Vancouver, BC, Canada; July 2008. p. 775–81.
- [22] Tang CJ, Patel VC, Landweber L. Viscous effects on propagation and reflection of solitary waves in shallow channels. *J Comput Phys* 1990;88(1):86–113.
- [23] Tang CJ, Chang JH. Flow separation during a solitary wave passing over a submerged obstacle. *J Hydra Eng* 1998;124(7):742–9.
- [24] Tang CJ, Chang JH. Application of local grid refinement to vortex motion due to a solitary wave passing over a submerged body. *Int J Num Meth Fluids* 2002;38:609–24.
- [25] Yih CS. Stream functions in three-dimensional flows. *La Houille Blanche* 1957;3:445–50. Also, Selected Papers by Chia-Shun Yih, editor. Lai WM, Lin SP. World Scientific II 1991; 893–8. (Langrange (1781) and Stokes (1842) were cited in this paper.)